

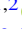









# Sodium Abundances in Very Metal-poor Stars

Yu-Fu Shen<sup>1,2</sup>, S. A. Alexeeva<sup>1</sup> , Gang Zhao<sup>1,2</sup> , Shuai Liu<sup>1,2</sup> , Zeming Zhou<sup>1,2</sup>, Hongliang Yan<sup>1,2</sup> , Haining Li<sup>1</sup> ,  
Tianyi Chen<sup>1,2</sup> , Xiaodong Xu<sup>1,2</sup>, Huiling Chen<sup>3,4</sup>, Huawei Zhang<sup>3,4</sup> , and Jianrong Shi<sup>1</sup> 

<sup>1</sup> CAS Key Laboratory of Optical Astronomy, National Astronomical Observatories, Chinese Academy of Sciences, Beijing 100101, China; [gzhao@nao.cas.cn](mailto:gzhao@nao.cas.cn), [hlyan@nao.cas.cn](mailto:hlyan@nao.cas.cn), [sjr@bao.ac.cn](mailto:sjr@bao.ac.cn)

<sup>2</sup> School of Astronomy and Space Science, University of Chinese Academy of Sciences, Beijing 100049, China

<sup>3</sup> Department of Astronomy, School of Physics, Peking University, Beijing 100871, China

<sup>4</sup> Kavli Institute for Astronomy and Astrophysics, Peking University, Beijing 100871, China

Received 2023 March 20; revised 2023 April 7; accepted 2023 April 11; published 2023 June 20

## Abstract

Chemical composition of very metal-poor (VMP) stars can provide observational constraints on current models of nucleosynthesis and the chemical evolution of the Galaxy. It has been found that the scatter of [Na/Fe] versus [Fe/H] in VMP stars is very large in contrast with most other elements. Moreover, a negative slope in [Na/Fe] versus [Fe/H] was found for giants, which is very unlikely according to the theory of nucleosynthesis. For the sample of 93 VMP stars in the metallicity range  $-4.25 < [\text{Fe}/\text{H}] < -1.64$  we obtained NLTE sodium abundances using the line profile fitting method by employing accurate atmospheric parameters determined when taking into account NLTE line formation for both Fe I and Fe II. Originally selected from the LAMOST low-resolution spectral database, the spectra of stars were obtained with the High Dispersion Spectrograph of the Subaru Telescope. For 57 turn-off stars in metallicity domain  $-3.04 < [\text{Fe}/\text{H}] < -1.64$ , we obtained mean  $[\text{Na}/\text{Fe}] = -0.29 \pm 0.14$  and positive slope  $0.09 \pm 0.06$ . For 21 giants distributed over metallicity  $-3.59 < [\text{Fe}/\text{H}] < -2.19$ , we found mean  $[\text{Na}/\text{Fe}] = -0.35 \pm 0.1$  and positive slope  $0.07 \pm 0.07$ . Our [Na/Fe] trend is lower by  $\sim 0.2$  dex, compared to the modern GCE model. We believe the GCE model should be adjusted, by considering the associated scatter. Twelve stars in our sample are found to be outliers, with too low or too high Na abundances.

*Key words:* techniques: spectroscopic – stars: abundances – stars: atmospheres

## 1. Introduction

The very metal-poor (VMP) stars are considered to be among the oldest stars in the universe, as they are believed to have formed from the remnants of the first generation of stars that died in supernova explosions. These early stars were composed mostly of hydrogen and helium, with minimal amounts of heavy elements. The supernova explosions of these stars enriched the interstellar medium with heavy elements, which later generations of stars incorporated into their atmospheres. Therefore, studying VMP stars can provide important clues about the early universe and the processes of stellar and Galactic evolution (Beers & Christlieb 2005; Frebel & Norris 2015; Nissen & Gustafsson 2018; Helmi 2020). Specifically, VMP stars are defined as having a metallicity less than about one-hundredth that of the Sun ( $[\text{Fe}/\text{H}] < -2.0$ ).

Sodium ( $z = 11$ , Na) is an odd- $Z$  element, mainly produced by Type II supernovae (Kobayashi et al. 2020) and its production increases with increasing metallicity. Determining the sodium (Na) abundance in VMP stars is an important step in understanding the early universe and the processes by which galaxies and stars have evolved over time. The relative abundance of sodium to iron can provide insights into the conditions under which the first stars formed, as well as the

mechanisms by which heavy elements were synthesized and distributed throughout the Galaxy. Understanding the abundance and distribution of sodium in VMP stars can help shed light on the processes by which galaxies and their constituent stars evolve over time.

Precision spectroscopy provides accurate and detailed information on VMP stars. Many spectroscopic campaigns have been conducted to study the chemical composition of VMP stars. The studies mainly focus on the abundance trends of  $[\text{X}/\text{Fe}]$  versus  $[\text{Fe}/\text{H}]$  for particular chemical element X, because these trends provide observational constraints on current models of nucleosynthesis and the chemical evolution of the Galaxy (e.g., Spite & Spite 1978; McWilliam et al. 1995; Cayrel et al. 2004; Kobayashi et al. 2006; Bensby et al. 2014; Zhao et al. 2016). Despite the large number of studies that have been conducted on the chemical abundances of stars, the problem of star-to-star scatter and systematic abundance shifts remains an active area of research in this field (Griffith et al. 2023).

Sodium is one of the elements with the biggest star-to-star scatter about the mean trend in VMP stars. As an example, in a recent study by Lombardo et al. (2022), a significant scatter of 0.17 dex was reported for sodium in a sample of 52 giant stars

spanning a metallicity range of  $-3.59 < [\text{Fe}/\text{H}] < -1.79$ . Li et al. (2022) studied a sample of VMP stars spanning a metallicity range of  $-4.3 < [\text{Fe}/\text{H}] < -1.7$  and reported a scatter of approximately 0.2 dex for  $[\text{Na}/\text{Fe}]$  when measuring the dispersion around a linear fit. Andrievsky et al. (2007) investigated 53 stars in the  $-4.2 < [\text{Fe}/\text{H}] < -1.6$  metallicity range and found in the turn-off stars and “unmixed” giants:  $[\text{Na}/\text{Fe}] = -0.21 \pm 0.13$ . However, when excluding mixed giants, whose atmospheres may have been polluted by sodium during their evolution, the scatter for the entire sample of stars (36 stars) was found to be larger with  $[\text{Na}/\text{Fe}] = -0.17 \pm 0.19$ .

The dispersion observed in average trends can arise from different enrichment events, such as those from core-collapse supernovae (CCSNe), Type Ia supernovae (SNe Ia), or asymptotic giant branch (AGB) stars. Measuring the intrinsic scatter can give an idea of the number and variety of enrichment events, the degree of mixing in the interstellar medium and the mixing of stellar populations with different enrichment histories (Vincenzo et al. 2021).

Another reason for this scatter is that measuring the chemical abundances of stars is a complex and challenging task, and different methods and assumptions can lead to different results. For example, different studies may use different techniques for measuring abundances, leading to discrepancies in the derived abundances. The discrepancies can be due to spectral normalization, stellar parameters, and atomic data like oscillator strengths.

It appears that another issue is prevalent among the studies, namely, negative slope of  $[\text{Na}/\text{Fe}]$  along the  $-2.8 \leq [\text{Fe}/\text{H}] \leq -1.5$ . For example, a negative slope of  $[\text{Na}/\text{Fe}]$  ( $-0.02 \pm 0.08$ ) is reported by Reggiani et al. (2017) in a sample of 23 metal-poor stars. It is highly unlikely to observe a negative slope in the evolution of  $[\text{Na}/\text{Fe}]$  since the production of sodium heavily depends on the initial metallicity of the progenitor stars. The authors suggested that the problem may be related to issues with non-local thermodynamic equilibrium (NLTE) treatment of the data. Similar negative slopes of  $[\text{Na}/\text{Fe}]$  were reported in other studies (e.g., Li et al. 2022:  $-0.11 \pm 0.07$  for giants).

NLTE effects are known to have a substantial influence on the spectral lines, particularly on the Na I resonance lines at 5890 and 5896 Å, which are commonly used for measuring the Na abundances in VMP stars. NLTE effects can lead to an overestimation of the Na abundance when using local thermodynamic equilibrium (LTE)-based analyses, especially in metal-poor giants where NLTE effects are more pronounced (e.g., Li et al. 2022; Lombardo et al. 2022). The NLTE approach can help to reduce systematic errors in the derived Na abundances.

In this study, we present the Na abundances in a sample of 93 VMP stars by employing their high-resolution spectra and following an accurate analysis technique. The sample is

selected starting from Aoki et al. (2022), Li et al. (2022). The sample is comprised of a range of 67 turnoff stars and 26 giants, uniformly distributed across the  $-4.3 \leq [\text{Fe}/\text{H}] \leq -1.5$  metallicity range, which is appropriate for research into Galactic chemical evolution (GCE).

A consistent set of effective temperatures ( $T_{\text{eff}}$ ), surface gravities ( $\log g$ ), metallicities, and microturbulence velocities ( $\xi_{\text{mic}}$ ) was obtained using lines from two ionization stages of iron, Fe I and Fe II. Our study benefits from taking into consideration the NLTE line formation for both Fe I and Fe II. NLTE line profile fitting is employed to determine the abundance of each individual Na I line, with departure coefficients calculated for the specific physical parameters of the star using classical one-dimensional (1D) model atmospheres. The model atom for Na I used in this work was treated and tested by Alexeeva et al. (2014).

Our goal is to minimize observational scatter and measure the intrinsic scatter as accurately as possible. We analyze outliers, such as Na-rich and Na-poor stars, to determine the possible reasons for their “anomalous” abundance.

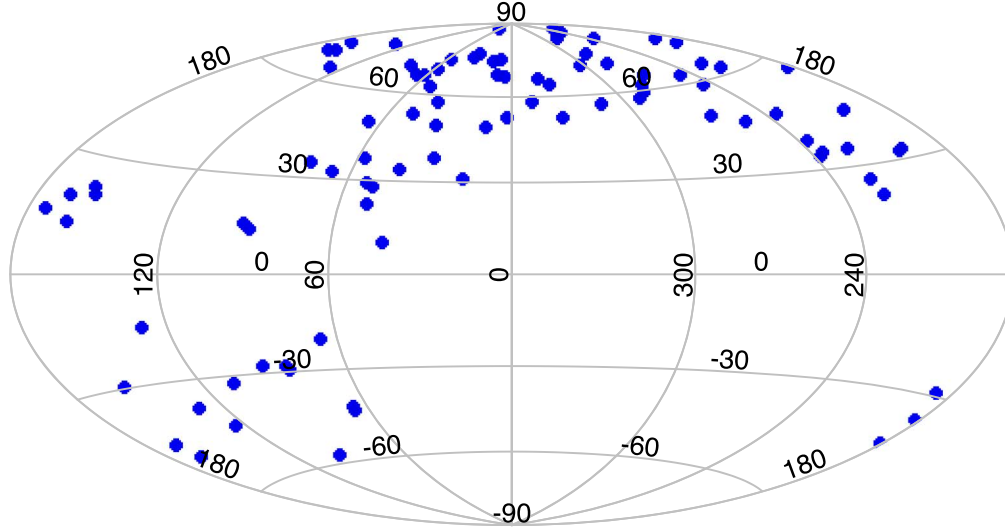
The paper is organized as follows. Section 2 describes the observation of the spectra, target selection, and the stellar parameters we used. Section 3 addresses the determination of Na abundance. Section 4 discusses the GCE. The conclusions are given in Section 5.

## 2. Observations, Parameters, and Stellar Sample

### 2.1. Observations

Our sample of VMP stars was selected from the Large sky Area Multi-Object fiber Spectroscopic Telescope (LAMOST, Zhao et al. 2006; Cui et al. 2012; Zhao et al. 2012; Liu et al. 2015; Yan et al. 2022) low-resolution ( $R \sim 2000$ ) spectroscopic database as metal-poor candidates (Li et al. 2018) and followed up with high-resolution spectroscopy (Aoki et al. 2022; Li et al. 2022) utilizing the High Dispersion Spectrograph (HDS) of the Subaru Telescope (Noguchi et al. 2002; Sato et al. 2002) through the JSPS-CAS Joint Research Program. High-resolution ( $R = 36,000$ ) spectra have wavelength range 4030–6800 Å with signal-to-noise ratio (SNR) more than 60.

We determine the locations of our sample stars based on the parallaxes given by Gaia Data Release 3 (DR3, Gaia Collaboration et al. 2016, 2022). We first convert the coordinates to Cartesian coordinates with the Sun as the center, and then make the Galactic center the coordinate center through translation. The Sun is placed at  $x = -8$  and  $y = z = 0$ . The Galactic locations of our sample are depicted in Figure 1. The positions of the stars in the  $x$ - $y$  and the  $z$ - $r_{\text{GC}}$  planes are also displayed in Figure 2. The star J1313-0552 (#51) is not included in Figure 2 due to extremely outlying coordinates. Coordinates and information about observations can be found in Table A1.



**Figure 1.** The locations for our sample of stars in the Galactic coordinates.

## 2.2. Stellar and Kinematic Parameters

Stellar parameters  $T_{\text{eff}}$ ,  $\log g$ , and  $\xi_{\text{mic}}$  were determined in this study applying different methods, including the spectroscopic one based on the NLTE analysis of lines of Fe I and Fe II. The stellar and kinematic parameters are listed in Table B1. The details of the determination of stellar parameters will be reported in Shi et al. (2023, in preparation).

The kinematic parameters: parallax, proper motion, and radial velocity are taken from Gaia DR3. A few radial velocities of stars are not provided by Gaia, so we use the radial velocities determined by spectra instead. We focus on space velocity components ( $U$ ,  $V$ ,  $W$ ), whose calculation is based on Johnson & Soderblom (1987). According to Figure 3, 16 stars within the circle with radius  $180 \text{ km s}^{-1}$  can be referred to as belonging to the thick disk, while the remaining 77 stars belong to the Galactic halo (Venn et al. 2004). The star J1313-0552 (#51) is not included in Figure 3 due to its extremely high velocity components ( $U = -1695 \text{ km s}^{-1}$ ,  $V = -84 \text{ km s}^{-1}$ ,  $W = 85 \text{ km s}^{-1}$ ).

## 2.3. Stellar Sample

We have 93 metal-poor stars with metallicity range  $-4.25 < [\text{Fe}/\text{H}] < -1.64$ . Most of our sample stars (88) are in the metallicity range  $-3.14 < [\text{Fe}/\text{H}] < -1.64$ .

Among 93 stars, 26 of them are giants and another 67 are turn-off stars. The  $T_{\text{eff}}\text{--}\log g$  diagram is shown in Figure 4.

## 3. NLTE Sodium Abundance

### 3.1. Method of Calculation

The 1D model atmospheres for given  $T_{\text{eff}}$ ,  $\log g$ , and  $[\text{Fe}/\text{H}]$  were calculated using the code MARCS (Gustafsson et al. 2008).

The opacity-sampling (OS) code is based on the opacity distribution function (ODF) version of Gehren (1979).

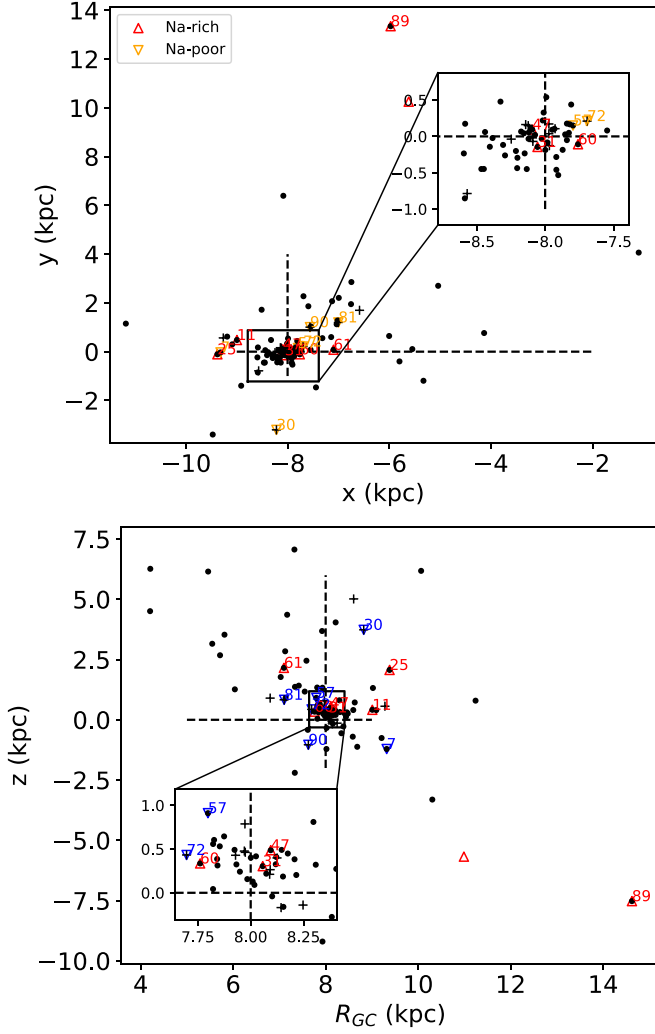
The model atom of Na I and the adopted atomic data are described in Alexeeva et al. (2014). To solve the radiative transfer and statistical equilibrium equations, we used the code DETAIL (Butler & Giddings 1985) based on the accelerated  $\Lambda$ -iteration method (Rybicki & Hummer 1991). Theoretical NLTE spectra were calculated with the code SYNTHV\_NLTE (Tsymbol et al. 2019) using the obtained departure coefficients  $b_i = n_{\text{NLTE}}/n_{\text{LTE}}$ . Here,  $n_{\text{NLTE}}$  and  $n_{\text{LTE}}$  are the statistical equilibrium and thermal (Saha–Boltzmann) number densities, respectively.

To examine theoretical stellar spectra and compare them to observations we employed widget program BINMAG<sup>5</sup> (Kochukhov 2018). BINMAG interfaces with mounted code SYNTHV\_NLTE which allows obtaining the best LTE and NLTE fits to the observed line profiles automatically to determine chemical abundances with high precision.

### 3.2. NLTE Sodium Abundance

In spectra of VMP stars, only the resonance doublet of Na I lines at  $5889.95$  and  $5895.92 \text{ \AA}$  can be used to measure Na abundance. The adopted atomic data for these lines are given in Table 1. Both LTE and NLTE abundances were derived using line profile fitting. Figure 5 illustrates the quality of the fits for  $5889 \text{ \AA}$  and  $5895 \text{ \AA}$  lines in three representative stars: J0119+2425 ( $T_{\text{eff}}/\log g/[\text{Fe}/\text{H}] = 6412/4.27/-2.56$ ), J0232+0545 ( $6091/4.08/-2.16$ ), and J0626+6032 ( $5926/3.77/-2.18$ ). It is worth noting that in some cases only one Na I line is available, because the second line is affected by

<sup>5</sup> <http://www.astro.uu.se/~oleg/binmag.html>



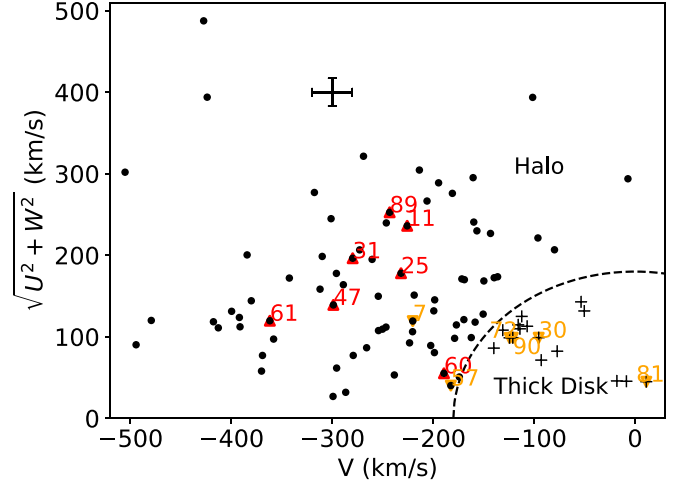
**Figure 2.** The positions of the VMP stars in the  $x$ - $y$  plane (upper panel) and the  $z$ - $r_{GC}$  plane (bottom panel), where  $x$ ,  $y$  and  $z$  are the directions of the Cartesian system of Galactic coordinates, and  $r_{GC} = \sqrt{x^2 + y^2}$ . The Sun is located at the intersection of the dashed lines ( $x = -8$ ,  $y = 0$ ,  $z = 0$ ). Some special stars are marked by the numbers. The number of the star follows its number from Table A1.

interstellar medium NaI lines. The lines with visual asymmetry were discarded. The deduced abundances of 93 VMP stars are listed in Table C1. An error = 0.0 means that the error is less than 0.01. The trend of  $[\text{Na}/\text{Fe}]$  along  $[\text{Fe}/\text{H}]$  is displayed in Figure 6.

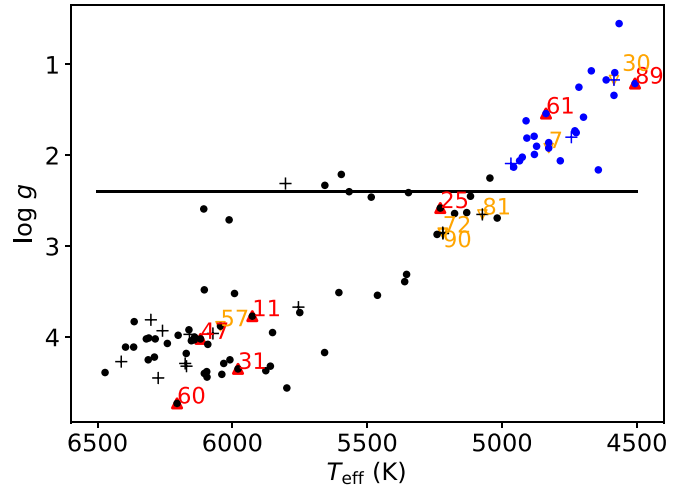
The NLTE  $[\text{Na}/\text{Fe}]$  abundances are lower than the LTE abundances, on average, by 0.46 dex. Average value of  $[\text{Na}/\text{Fe}]_{\text{NLTE}} = -0.28 \pm 0.23$ , while  $[\text{Na}/\text{Fe}]_{\text{LTE}} = +0.18 \pm 0.32$ . Applying the NLTE approach leads to a decrease in the error of the average value for  $[\text{Na}/\text{Fe}]$ .

### 3.3. Abundance Uncertainties

We calculate the abundance uncertainties by changing parameters by  $+80$  K in  $T_{\text{eff}}$ ,  $+0.07$  dex in  $\log g$ ,



**Figure 3.**  $UVW$  velocity diagram for our sample of stars, except for #51. The dashed line is part of a circle whose radius is  $180 \text{ km s}^{-1}$ . The markers are the same as Figure 2.

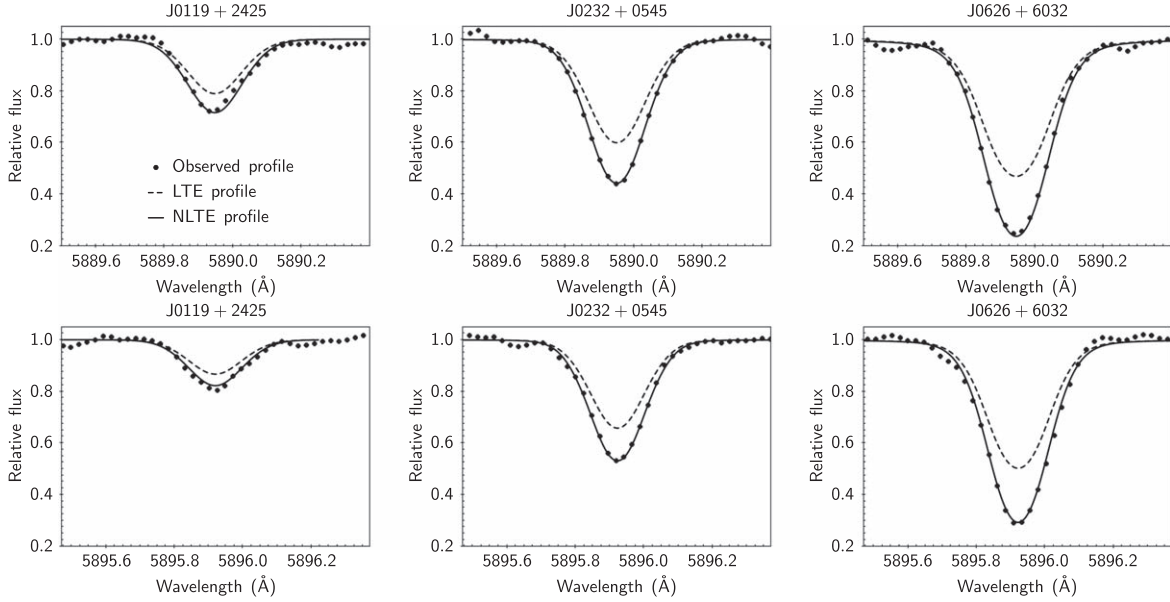


**Figure 4.**  $T_{\text{eff}}$  versus  $\log g$  of 93 stars. The solid line is  $\log g = 2.4$ , which is the most important basis for distinguishing between giants (blue) and turn-off stars (black). The other markers are the same as in Figure 2.

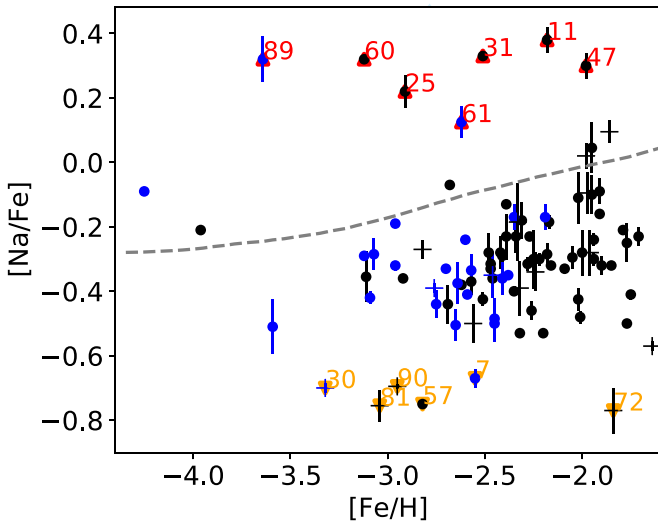
**Table 1**  
The Line List Used in this Work

$\lambda$ ( $\text{\AA}$ )	$\log gf$	$E_{\text{ex}}$ (eV)	$\log \gamma_{\text{rad}}$	$\log \frac{\gamma_{\text{star}}}{N_e}$	$\log \frac{\gamma_{\text{vdW}}}{N_{\text{H}}}$	$\log \epsilon_{\odot/\text{Na}}$
5889.95	0.109	0.00	7.799	-5.87	-7.52	6.17
5895.92	-0.194	0.00	7.798	-5.87	-7.5	6.17

and  $+0.1 \text{ km s}^{-1}$  in  $\xi_{\text{mic}}$  in atmospheres of two stars J1432 +3755 (4585/1.34/ $-3.12$ ) and J0244+0828 (6472/4.39/ $-2.26$ ) (Table 2). These two stars are from our sample with the highest and lowest temperature we chose as an example.



**Figure 5.** Best NLTE fits (solid curves) of the observed spectra of three representative stars (filled circles). The LTE profiles were computed with the corresponding NLTE abundances and are shown by dashed curves.



**Figure 6.** [Na/Fe] versus [Fe/H] determined in this work. The gray dashed line is the GCE model from Kobayashi et al. (2020). The markers are the same as in Figure 4.

The total error was calculated by assuming all of the individual errors to be independent. In the atmosphere of a cool giant, the errors in [Na/Fe I] due to the uncertainties in  $T_{\text{eff}}$  and  $\log g$  are small compared to those of a hotter dwarf.

### 3.4. Test on Determination of Sodium Abundances

We test the robustness of our sodium abundance determination to ensure the accuracy and reliability of our determination

**Table 2**

Sensitivity of the [Na/Fe] Abundance to the Atmospheric Parameters,  $\Delta \log \epsilon_{\text{Na}}$ , For Two Representative Stars, J1432+3755 (4585/1.34/−3.15) and J0244+0828 (6472/4.39/−2.26)

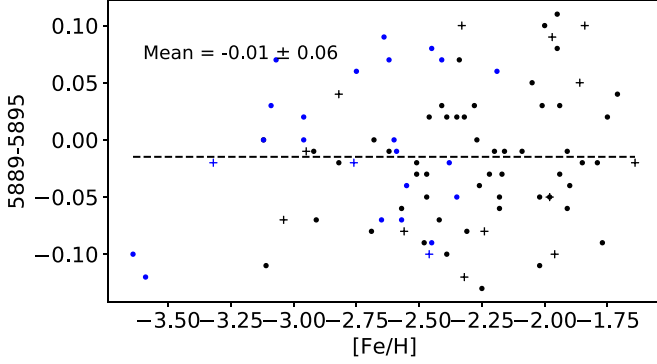
Name	$\Delta T_{\text{eff}}$ +80 K	$\Delta \log g$ +0.07	$\Delta \xi_{\text{mic}}$ +0.1 km s <sup>−1</sup>	Total
J1432+3755	+0.05	0.00	−0.03	0.06
J0244+0828	+0.09	+0.07	+0.04	0.12

of sodium abundances in stars. Figure 7 displays differences in the Na abundances obtained from the two Na I lines used in this study. The abundances obtained from two lines show good agreement, with differences typically below 0.06 dex. However, there may be a very weak dependence of the [Na/Fe] on  $T_{\text{eff}}$  and  $\xi_{\text{mic}}$  (Figure 8).

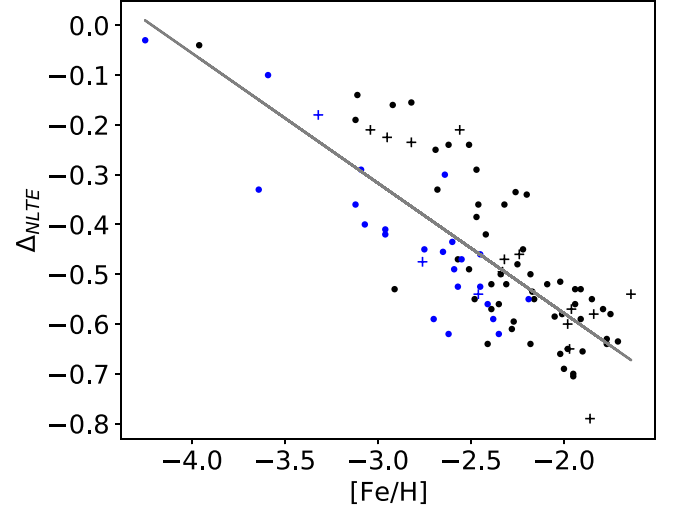
### 3.5. Differences Between LTE and NLTE

For our sample of stars, the NLTE abundance effects (defined as  $\Delta_{\text{NLTE}} = \log \epsilon_{\text{NLTE}} - \log \epsilon_{\text{LTE}}$ ) for both lines, 5889.95 and 5895.92 Å, are from −0.03 to −0.79 dex, depending on the stellar parameters. NLTE abundance effects mainly depend on metallicity (Figure 9). They are small if  $[\text{Fe}/\text{H}] < -3.5$  and become larger in absolute value with increasing  $[\text{Fe}/\text{H}]$  from −3.5 to −2.0 dex. On one hand, in metal-poor stars, the density of particles is low so particles collide insufficiently, and the NLTE effect should be stronger. The difference between LTE and NLTE of metal-poor stars is much stronger than relatively metal-rich stars, which could be

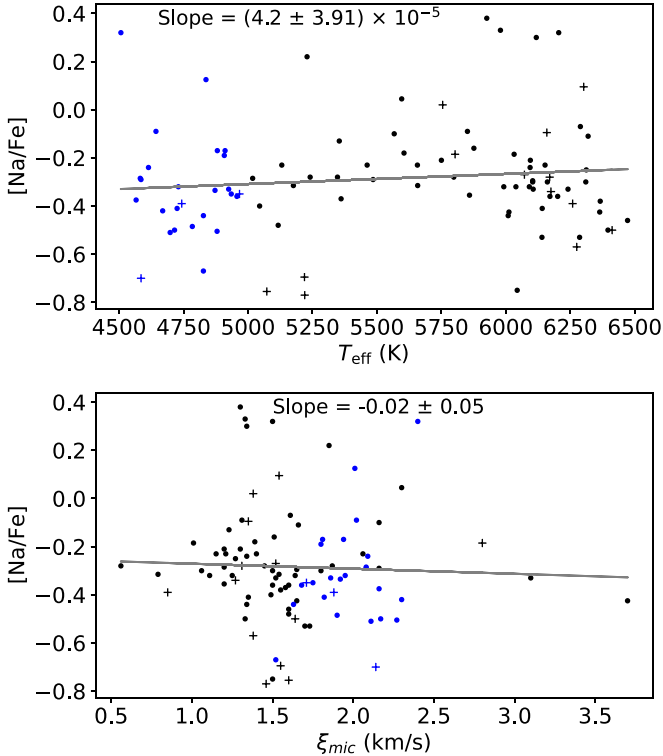




**Figure 7.** “5889–5895” means  $A(\text{Na I } 5889.95 \text{ \AA}) - A(\text{Na I } 5895.92 \text{ \AA})$ . The dashed line shows the average. The markers are the same as in Figure 4.



**Figure 9.**  $\Delta_{\text{NLTE}}$  versus  $[\text{Fe}/\text{H}]$ . The line is the linear fit. The markers are the same as in Figure 4.



**Figure 8.**  $[\text{Na}/\text{Fe}]$  as a function of  $T_{\text{eff}}$  (upper panel) and  $\xi_{\text{mic}}$  (bottom panel). The solid lines represent linear fits. The markers are the same as in Figure 4.

found in previous works (e.g., Gehren et al. 2006). On the other hand, with low metallicity, the line formation region for investigated lines is moving toward deeper layers, where LTE prevails. Below, we present an explanation of why in the atmospheres with  $[\text{Fe}/\text{H}] < -3.5$  NLTE effects become weaker.

Figure 10 presents the departure coefficients for the three Na I levels in the atmospheres of two stars, J1231+5243

(5755/3.67/−1.98) and J1253+0753 (5750/3.73/−3.96). The stars have close  $T_{\text{eff}}$  and  $\log g$ , and the difference in  $[\text{Fe}/\text{H}]$  is almost 2.0 dex. It allows us to focus on the metallicity effect.

We know that flux depends on two functions: the source function  $S_\nu$  and the optical depth  $\tau_\nu$ . For lines in the visual and ultraviolet (UV) region, we have

$$S_\nu \sim B_\nu(T) \frac{b_u}{b_l}, \quad (1)$$

where  $B_\nu$  is the Planck function, and  $b_u$  and  $b_l$  are departure coefficients for the upper (u) and lower (l) energy levels for transition  $l \rightarrow u$  respectively.

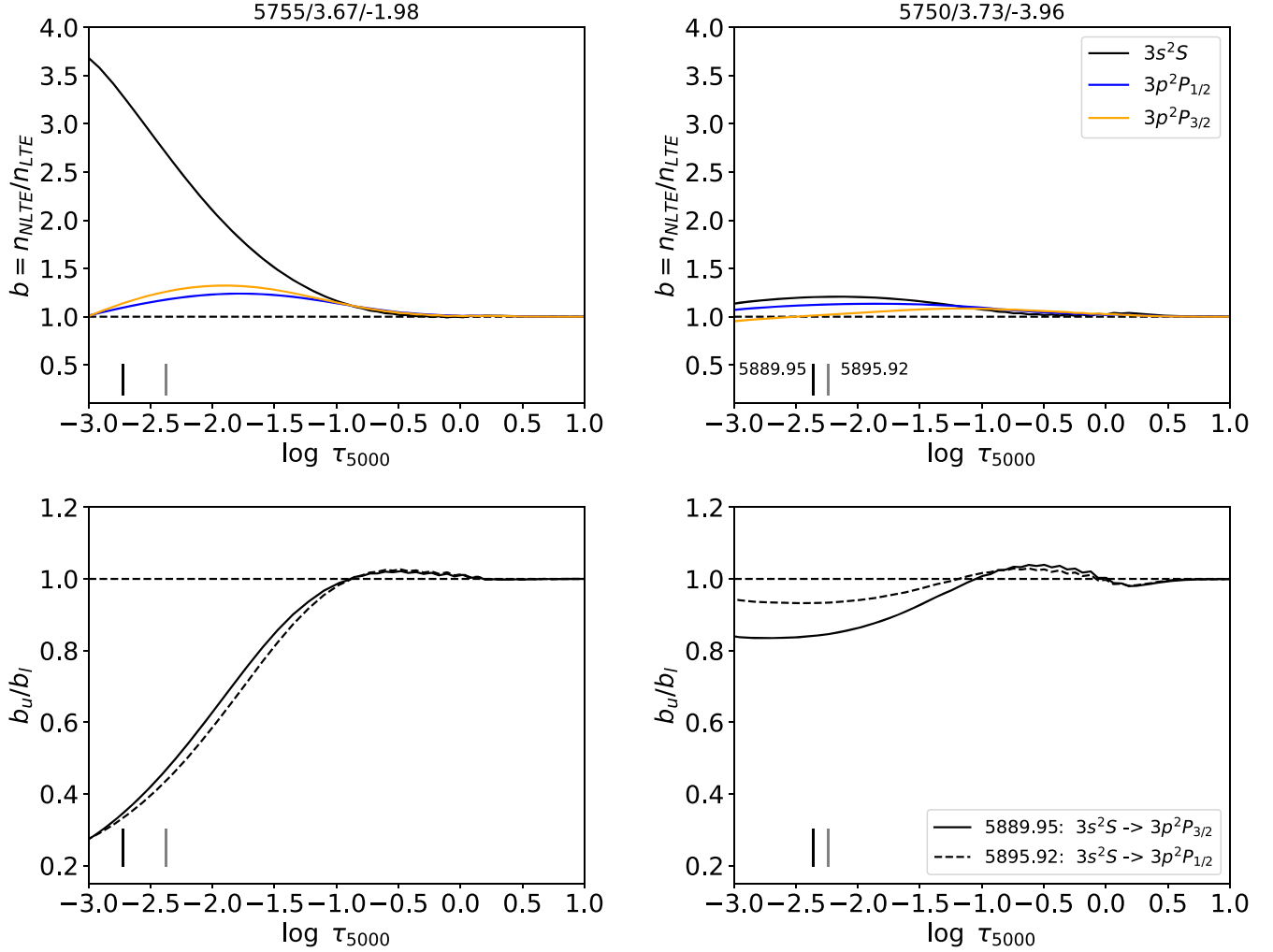
In addition,  $\tau_\nu$  depends on opacity  $\chi_\nu$ , and we have

$$\chi_\nu \sim b_l n_l^{\text{LTE}} \left( 1 - \frac{b_u}{b_l} e^{-\frac{h\nu}{kT}} \right) \sim b_l, \quad (2)$$

so, when  $b_l > 1$  and (or)  $b_u/b_l < 1$ , an NLTE strengthening of the line occurs.

As shown in the left panels of Figure 10, in model atmosphere 5755/3.67/−1.98, the Na I line at 5889 Å forms in layers around  $\log \tau_{5000} = -2.75$ , where  $b_l = 3.4$ , and  $b_u/b_l = 0.32 < 1$ . Both factors lead to a strengthening line in NLTE, and  $\Delta_{\text{NLTE}} = -0.56$  for the line at 5889 Å.

In the model atmosphere 5750/3.73/−3.96, the Na I line at 5889 Å forms in deeper layers around  $\log \tau_{5000} = -2.4$ , where  $b_l = 1.25$ , and  $b_u/b_l = 0.82 < 1$ , and both factors also lead to a strengthening line in NLTE, and  $\Delta_{\text{NLTE}} = -0.04$ . The absolute value of  $\Delta_{\text{NLTE}}$  becomes less with decreasing metallicity from −2.0 to −3.0 dex, because (1) the line formation of Na I lines moves toward deeper layers, where NLTE effects are weaker; (2) the departure coefficients of the lower level drop to smaller values.



**Figure 10.** Departure coefficients  $b$  and  $b_u/b_l$  (upper level / lower level) for Na I versus optical depth. The parameters of the models are given on the top of the panels, in  $T_{\text{eff}}$  (K)/ $\log g$ /[Fe/H] format. Two vertical lines indicate the line formation regions for the cores of Na I 5889.95 and 5895.92 Å lines.

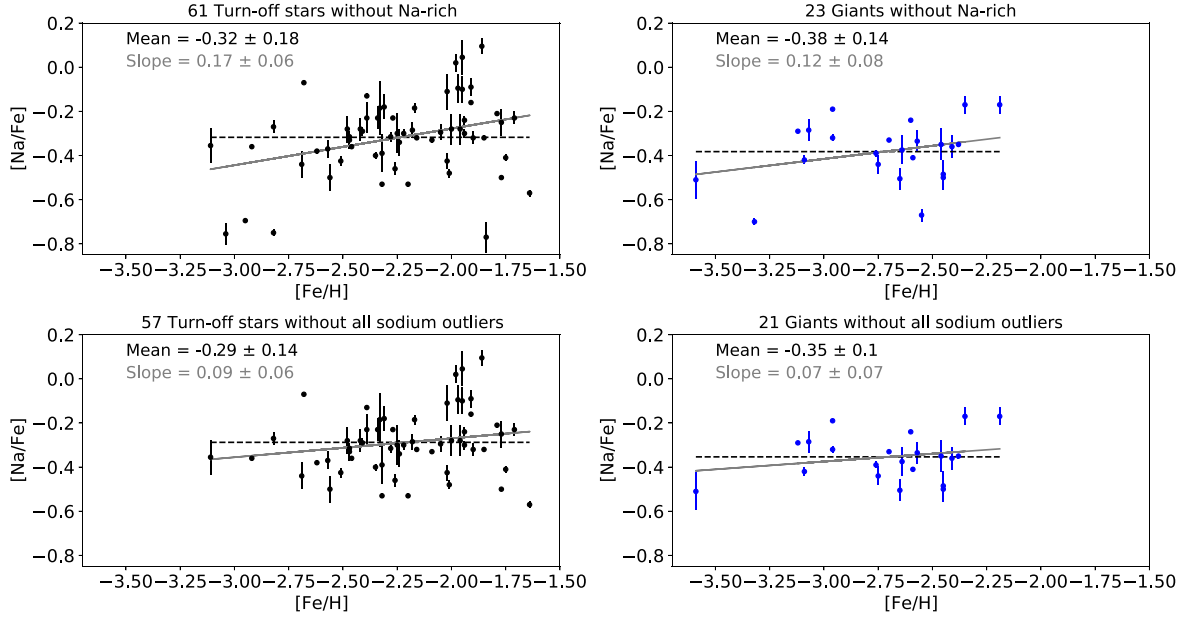
#### 4. The Galactic Chemical Evolution

The abundance trend of [Na/Fe] versus [Fe/H] determined in this work is shown in Figure 6. We compare our result with the GCE model (gray dashed line) from Kobayashi et al. (2020). GCE models consider that [Na/Fe] and [Fe/H] are positively correlated in metal-poor stars. We examine the slopes and mean [Na/Fe] values in the sample of stars, which was segregated into turn-off and giant stars (Figure 11). Some outliers are considered when examining the slopes and mean values. Stars with  $[\text{Na}/\text{Fe}] \geq +0.1$  are named “Na-rich” and stars with  $[\text{Na}/\text{Fe}] \leq -0.67$  are named “Na-poor.” For turn-off stars within the metallicity range of  $-3.04$  to  $-1.64$ , we determine a slope of  $0.17 \pm 0.06$  when excluding only Na-rich stars, and a slope of  $0.09 \pm 0.06$  when excluding all outliers. The mean value of [Na/Fe] does not depend much on whether we take into account Na-poor stars or not and consists of

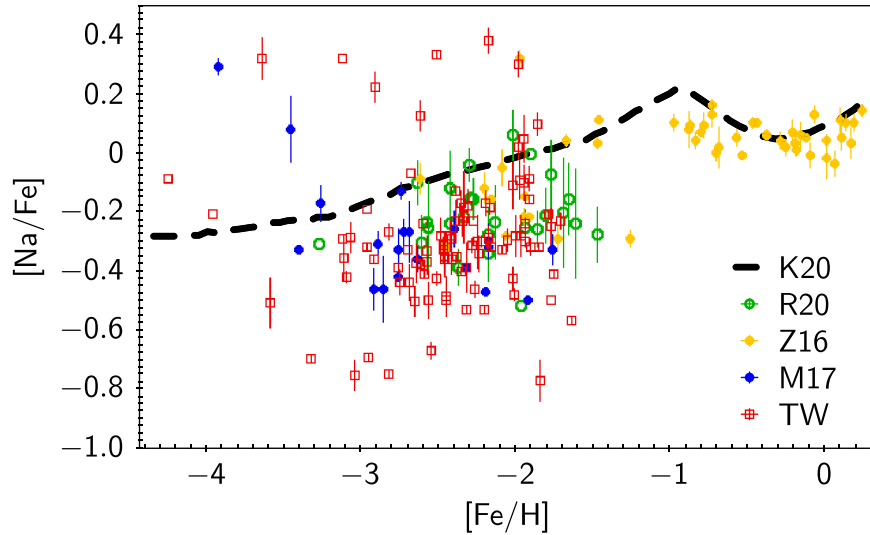
$-0.32 \pm 0.18$  and  $-0.29 \pm 0.14$ , respectively. A similar result is obtained for giants. In the sample of 23 giants (Na-rich stars are excluded) in metallicity range  $-3.64 < [\text{Fe}/\text{H}] < -2.19$ , the slope is  $0.12 \pm 0.08$  with mean value  $-0.38 \pm 0.14$ . The scatter decreases after excluding two Na-poor stars resulting in the slope  $0.07 \pm 0.07$  and mean [Na/Fe] is  $-0.35 \pm 0.1$ . All obtained slopes are positive and results for turn-off stars and giants are consistent within the error bars.

The star-to-star standard deviation of [Na/Fe] in this work is 0.233 dex in case all 93 stars are taken into account. If we exclude the six Na-rich stars and the six Na-poor stars mentioned in Section 4.2, the scatter is reduced to 0.14 dex. However, even if the scatter is  $\sim 0.14$  dex, it is still larger than the scatter for stars with  $[\text{Fe}/\text{H}] > -1.5$ .

The abundance of Na is heavily influenced by the progenitor stars, but since progenitor stars can only contaminate nearby



**Figure 11.**  $[\text{Na}/\text{Fe}]$  versus  $[\text{Fe}/\text{H}]$  in our sample stars, segregated into turn-off (left panels) and giant (right panels) stars. Two stars with  $[\text{Fe}/\text{H}] < -3.7$  are excluded. The linear fits (gray solid lines) and averages (black dashed lines) of them are given.

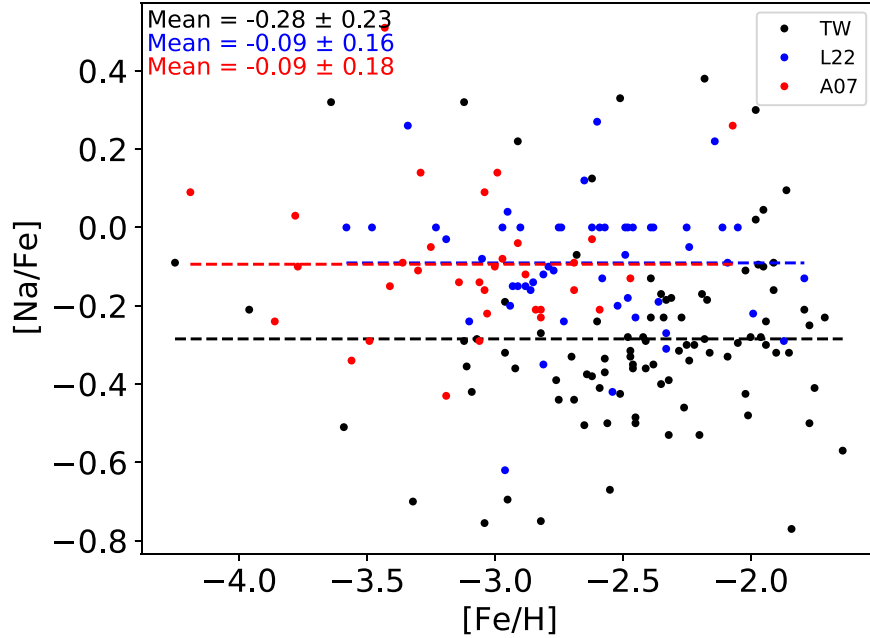


**Figure 12.**  $[\text{Na}/\text{Fe}]$  versus  $[\text{Fe}/\text{H}]$  for our sample stars is marked by red squares (TW means this work). For comparison, we present data from literature: M17: Mashonkina et al. (2017); Z16: Zhao et al. (2016); R20: Reggiani et al. (2017, 2020); and K20 is the GCE model given by Kobayashi et al. (2020).

gas, it takes time for the gas to mix on a large scale. During the formation of older stars, the gas may not be fully mixed, resulting in a large variance in abundances. This phenomenon applies to all elements, and it is a well-known fact that the abundances of many elements exhibit a similar trend, where stars with lower abundances tend to have larger scatter.

Considering the timescale of interstellar medium mixing can be valuable in enhancing the accuracy of GCE models. We have observed that the scatter of the sample is smaller at higher  $z$  compared to lower  $z$ , as demonstrated in Figure 15. It is possible to assume that the stars, which underwent stronger interactions and were pushed to higher  $z$ , experienced more





**Figure 13.** Comparison of our trend of  $[\text{Na}/\text{Fe}]$  versus  $[\text{Fe}/\text{H}]$  with data from literature. TW means this work, A07 is Andrievsky et al. (2007), and L22 is Lombardo et al. (2022). The averages are indicated by the dashed lines. One outlier ( $[\text{Na}/\text{Fe}] > 1.5$ ) of Andrievsky et al. (2007) is excluded.

thorough mixing of gas in their birth regions. It would require further investigation and analysis to confirm whether this is true or it is a selection effect.

Figure 12 displays our sample as well as samples from previous works, along with the prediction provided by the GCE model (Kobayashi et al. 2020). It appears that the GCE model overestimates the  $[\text{Na}/\text{Fe}]$  ratio in stars with  $[\text{Fe}/\text{H}]$  between  $-3.0$  and  $-2.0$ . In fact, this problem has already appeared in some of the previous samples; two previous works find a higher average (Andrievsky et al. 2007; Lombardo et al. 2022), and we will discuss this in detail in the next subsection.

#### 4.1. Test on HD 122563

The comparison between our NLTE sodium abundances in 93 VMP stars and those from literature, specifically 33 VMP stars from Andrievsky et al. (2007) and 52 VMP stars from Lombardo et al. (2022) are displayed in Figure 13. Our sample of 93 stars has a mean value of  $-0.28 \pm 0.23$ , which is 0.19 dex lower than the mean values reported in those two studies.

In order to gain a better understanding of the systematic shift observed in our  $[\text{Na}/\text{Fe}]$  abundances compared to Andrievsky et al. (2007), we conducted test calculations based on VMP star HD 122563 with well-determined stellar parameters (4600/1.40/-2.55/1.6). HD 122563 is widely recognized as a benchmark star, especially in the context of Gaia mission calibration and testing of spectroscopic and asteroseismic analysis techniques. This star is also presented in Andrievsky

et al. (2007), where different physical parameters were used, such as  $T_{\text{eff}} = 4600$  K,  $\log g = 1.1$ ,  $[\text{Fe}/\text{H}] = -2.82$ , and microturbulence =  $2.0 \text{ km s}^{-1}$ . Applying our method with the same physical parameters as Andrievsky et al. (2007), we found a value of  $[\text{Na}/\text{Fe}] = -0.20$  dex, very close to that of Andrievsky et al. (2007), who found  $[\text{Na}/\text{Fe}] = -0.23$  dex. It means that our NLTE treatment of Na I lines is similar to that used in the study by Andrievsky et al. (2007).

Using our adopted physical parameters of HD 122563 (4600/1.40/-2.55/1.6), we obtained an  $[\text{Na}/\text{Fe}]$  value of  $-0.31$  dex, which is 0.11 dex lower compared to the value reported by Andrievsky et al. (2007). If we compare the parameters between Andrievsky et al. (2007) and our study, we can see that the main difference is in the metallicity. In Andrievsky et al. (2007), the metallicity was 0.27 dex lower than in our study and an LTE abundance was used for iron. Underestimation of iron leads to an underestimation of  $[\text{Fe}/\text{H}]$  and an overestimation of  $[\text{Na}/\text{Fe}]$ . In addition, Lombardo et al. (2022) also determine NLTE Na abundances of 26 species, and reach an average that is consistent with Andrievsky et al. (2007), as affirmed in Figure 13. The parameters used in Andrievsky et al. (2007), Lombardo et al. (2022) are both LTE parameters.

The results of this test indicate that the systematic shift observed in the  $[\text{Na}/\text{Fe}]$  trend is primarily caused by differences in the sets of stellar parameters considered, particularly the metallicity derived from NLTE and LTE-based methods.

**Table 3**  
The List of Some Special Stars

No.	Name, LAMOST	Peculiarity	Comment
11	J0626+6032	Na-rich	Turn-off and halo
25	J1017+3755	Na-rich	Turn-off and halo
31	J1123+0937	Na-rich	Turn-off and halo
47	J1234+4201	Na-rich	Turn-off and halo
60	J1410-0555	Na-rich	Turn-off and halo
61	J1414+1457	Na-rich	Giant and halo
89	J2217+2104	Na-rich	Giant and halo
7	J0326+0202	Na-poor	Giant and halo
30	J1118-0650	Na-poor	Giant and Disk
57	J1401+2659	Na-poor	Turn-off and halo
72	J1548+2113	Na-poor	Turn-off and Disk
81	J1733+2633	Na-poor	Turn-off and Disk
90	J2221+0228	Na-poor	Turn-off and Disk
51	J1313-0552	Very high $z$ and very high velocity	Giant and halo

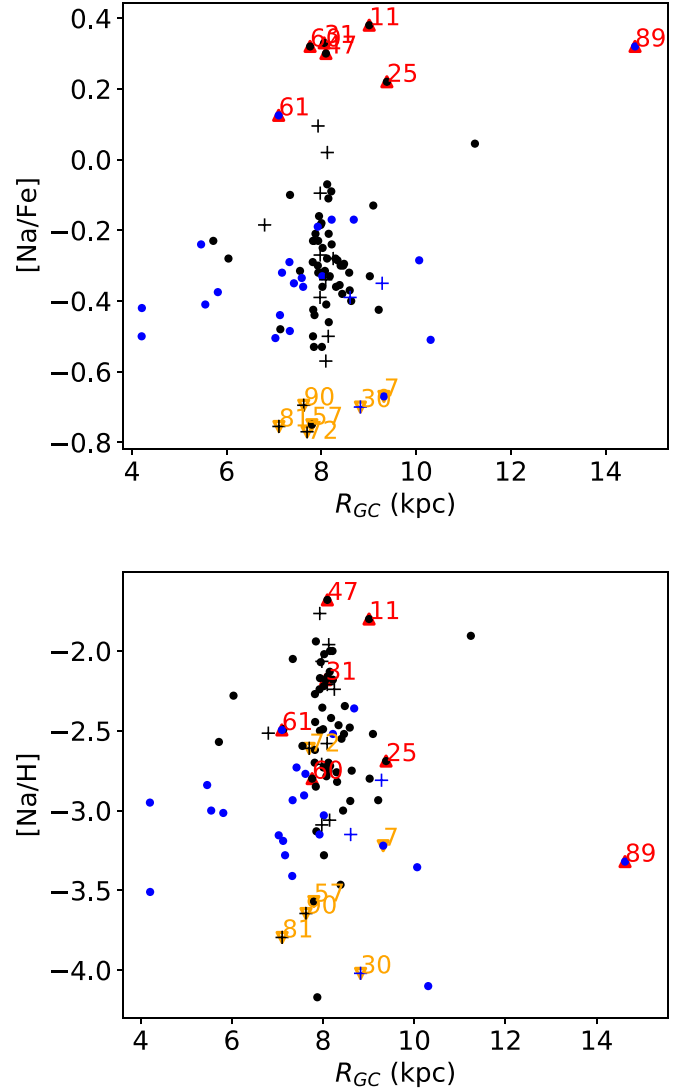
#### 4.2. Special Stars

We distinguish some outliers (Table 3). Seven stars with  $[\text{Na}/\text{Fe}] \geq +0.1$  appear to be “Na-rich” and six stars with  $[\text{Na}/\text{Fe}] \leq -0.67$  are identified as “Na-poor.”

Star #61 and 89 are two giants and suspected to have suffered a mixing between the atmosphere and the H-burning shell bringing the products of the Ne-Na cycle to the surface. Five out of six “Na-rich” stars are turn-off stars: #11, 25, 31, 47, and 60 (Figure 4). It is difficult to explain their sodium overabundance by an evolutionary effect. We analyzed their kinematics and positions. Figures 14, 15, and 16 respectively represent  $R_{\text{GC}}$ ,  $|z|$ , and total angular momentum ( $L = \sqrt{L_x^2 + L_y^2 + L_z^2}$ , where  $L_x = y*W - z*V$ ,  $L_y = z*U - x*W$ ,  $L_z = x*V - y*U$ ) versus  $[\text{Na}/\text{Fe}]$  and  $[\text{Na}/\text{H}]$  for our sample of stars. Four stars #11, 25, 31, and 47 are relatively close to each other on the  $UVW$  diagram (Figure 3); they have similar  $R_{\text{GC}}$ ,  $|z|$ , and  $L$ . We believe that they have merged from neighboring galaxies and their chemical enrichment history is different.

Another possible explanation of their sodium overabundance is that the stars have undergone a process of metallicity enrichment, where they have accreted material from a companion star that has already gone through nuclear fusion and produced sodium. This would result in an overabundance of sodium in the star’s atmosphere compared to other stars of similar age and mass. We have tried to find evidence that these stars are binaries. However, we have not yet found evidence that these stars are binaries. All seven Na-rich stars were excluded when calculating the average  $[\text{Na}/\text{Fe}]$  and slope of our sample.

Stars #7, 30, 57, 72, 81, and 90 are Na-poor stars. Four of them belong to the thick disk. They have lower velocity components than the other stars in our sample (Figure 3). They



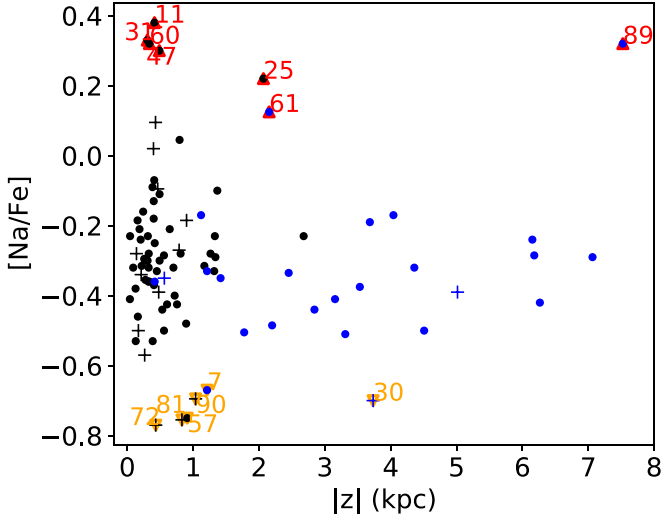
**Figure 14.**  $R_{\text{GC}}$  versus  $[\text{Na}/\text{Fe}]$  (upper panel) and  $[\text{Na}/\text{H}]$  (lower panel) for our sample of stars. The markers are the same as in Figure 4.

also have close  $L \sim 1000 \text{ km s}^{-1} \text{ kpc}$  (Figure 16). From above, we think those Na-poor stars may be old thick disk stars.

Star #51 was also included in the list of outliers. It is a giant with very high  $z = 70.73 \text{ kpc}$ , and extremely high velocity components. However, its  $[\text{Na}/\text{Fe}]$  is  $-0.09$ , which is very close to the vast majority of our sample. Star #51 is not shown in the diagrams involving coordinates or kinematic parameters.

## 5. Conclusion

Using accurate stellar parameters and high-resolution ( $R = 36,000$ ) stellar spectra obtained with the HDS of the Subaru Telescope, we calculated the NLTE sodium abundances in a sample of 93 stars with the  $-4.25 < [\text{Fe}/\text{H}] < -1.64$  metallicity range. The sample of stars used in this study allows



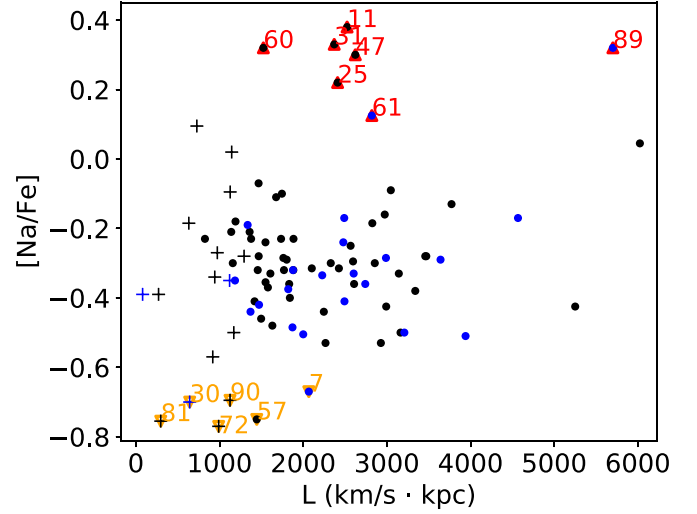
**Figure 15.**  $|z|$  versus  $[Na/Fe]$  (upper panel) and  $[Na/H]$  (lower panel) for our sample of stars. The markers are the same as in Figure 4.

us to trace the properties of the Galactic halo and thick disk stars. Based on kinematics, most of the stars (77) belong to the halo. This is the first study devoted to sodium in VMP stars homogeneously distributed in metallicity range from  $-4.2$  to  $-1.6$  dex appropriate for Galactic chemical evolution research.

The synthesis method was utilized to determine the NLTE sodium abundances for each individual NaI resonance line. Departure coefficients, which were calculated for the specific physical parameters of each star using classical 1D model atmospheres, were taken into account during the abundance determination process. It has been demonstrated that the abundance differences between NLTE and LTE are diminishing as metallicity decreases from  $-2$  to  $-4$ , which is in line with previous NLTE studies, e.g., Baumüller et al. (1998).

The abundance trend of  $[Na/Fe]$  versus  $[Fe/H]$  obtained in this study has positive slope in the  $[Fe/H]$  range of  $-3.04$  to  $-1.64$  that is in accordance with prediction of the GCE model. For two groups of stars, turn-off and giants, we found slopes,  $0.09 \pm 0.06$  and  $0.07 \pm 0.07$ , respectively. However, mean  $[Na/Fe]$  is lower than expected by the GCE model in the  $[Fe/H]$  range of  $-3.04$  to  $-1.64$ .

We believe there is an intrinsic scatter of Na abundances, so the GCE model needs to be adjusted, not only the average, but



**Figure 16.** Total angular momentum ( $L$ ) versus  $[Na/Fe]$  (upper panel) and  $[Na/H]$  (lower panel) for our sample of stars. The markers are the same as in Figure 4.

also considering the scatter. We have measured the intrinsic scatter as 0.14 dex for 57 turn-off stars in our sample and 0.12 dex for 21 giants.

Among 93 stars, we find 13 outliers: seven Na-rich stars and six Na-poor stars. Five Na-rich turn-off stars may have extragalactic origins, however, it is difficult to make a solid conclusion. We also find a VMP giant with extremely high velocity components and very high- $z$ . However, its sodium abundance is closer to the mean  $[Na/Fe]$  value obtained for the whole sample.

## Acknowledgments

This research was funded by the National Natural Science Foundation of China (NSFC, Grant Nos. 11988101 and 11890694), and the National Key R&D Program of China No. 2019YFA0405502. This work was based on observations carried out with the High Dispersion Spectrograph (HDS) of the Subaru Telescope through the JSPS-CAS Joint Research Program. We made use of the SIMBAD and VALD databases.

*Software:* DETAIL (Butler & Giddings 1985); SYNTHV\_NLTE (Tsymbal et al. 2019); BINMAG (Kochukhov 2018).

## Appendix A Sample Stars

**Table A1**  
Locations and Magnitudes of our Sample

No.	Name LAMOST	Obs.Date Y-m	R.A. (deg.)	Decl. (deg.)	G_Gaia (mag.)	x (kpc)	y (kpc)	z (kpc)	$R_{GC}$ (kpc)
1	J0055+1857	2016 Nov	13.864 525	18.965 879	10.83	-8.33	0.48	-0.56	8.34
2	J0119+2425	2016 Nov	19.871 023	24.425 343	11.61	-8.14	0.16	-0.17	8.14
3	J0131+4800	2017 Feb	22.816 286	48.004 845	10.04	-8.1	0.12	-0.04	8.1
4	J0232+0545	2015 Nov	38.209 171	5.751 286	13.79	-8.58	0.17	-0.7	8.59
5	J0244+0828	2017 Feb	41.146 194	8.480 548	11.27	-8.15	0.04	-0.16	8.15
6	J0246+2643	2015 Nov	41.678 204	26.724 737	11.42	-9.19	0.62	-0.76	9.21
7	J0326+0202	2015 Nov	51.724 506	2.041 151	11.57	-9.32	-0.03	-1.21	9.32
8	J0352+0514	2015 Nov	58.044 93	5.247 481	13.24	-8.38	-0.02	-0.28	8.38
9	J0423+0538	2017 Feb	65.886 482	5.647 117	12.02	-8.25	-0.04	-0.14	8.25
10	J0554+5235	2015 Nov	88.535 583	52.599 735	13.49	-11.18	1.15	0.79	11.24
11	J0626+6032	2015 Nov	96.699 631	60.548 325	13.82	-9.0	0.48	0.41	9.01
12	J0637+4308	2015 Nov	99.472 878	43.138 603	12.38	-8.44	0.06	0.13	8.44
13	J0643+5111	2015 Nov	100.771 423	51.190 083	13.11	-9.09	0.3	0.4	9.09
14	J0643+5934	2016 Nov	100.757 782	59.575 203	10.95	-9.27	0.56	0.56	9.28
15	J0828+0037	2016 May	127.042 976	0.618 464	12.5	-8.47	-0.45	0.26	8.48
16	J0832+2450	2016 May	128.242 981	24.833 618	12.05	-8.4	-0.14	0.27	8.41
17	J0834+2307	2016 May	128.703 873	23.126 23	12.15	-8.59	-0.23	0.41	8.6
18	J0845+0150	2016 May	131.279 48	1.836 369	12.93	-8.45	-0.45	0.31	8.46
19	J0913+0726	2016 May	138.307 617	7.437 215	12.62	-8.21	-0.2	0.2	8.22
20	J0924+2651	2016 May	141.204 529	26.863 159	11.87	-8.31	-0.12	0.32	8.31
21	J0934-0108	2016 May	143.536 697	-1.140386	11.71	-8.59	-0.85	0.72	8.63
22	J0934-0259	2016 May	143.657 944	-2.991637	12.33	-8.15	-0.23	0.19	8.15
23	J0948+0000	2016 May	147.039 215	0.002 265	11.87	-8.91	-1.4	1.32	9.02
24	J1014+0547	2016 May	153.604 08	5.791 098	12.22	-8.2	-0.29	0.38	8.21
25	J1017+3755	2016 May	154.495 132	37.932 514	12.71	-9.38	-0.11	2.07	9.38
26	J1044-0358	2016 May	161.045 639	-3.982261	12.84	-8.13	-0.45	0.49	8.15
27	J1050+2135	2016 May	162.538 91	21.592 579	11.27	-8.09	-0.07	0.21	8.09
28	J1101+2031	2017 Feb	165.455 795	20.523 861	11.27	-8.29	-0.26	0.81	8.3
29	J1109+0754	2014 May	167.255 096	7.911 607	12.06	-9.47	-3.4	6.18	10.06
30	J1118-0650	2016 Apr	169.649 49	-6.845829	11.27	-8.22	-3.21	3.73	8.82
31	J1123+0937	2016 May	170.977 737	9.628 229	12.53	-8.06	-0.15	0.3	8.06
32	J1123+3217	2016 May	170.951 157	32.286 118	11.75	-8.09	-0.02	0.26	8.09
33	J1135+3100	2016 May	173.825 165	31.006 306	12.28	-8.12	-0.03	0.41	8.12
34	J1137+4413	2016 May	174.316 238	44.222 752	12.21	-8.18	0.07	0.45	8.18
35	J1144+4032	2016 May	176.073 242	40.538 326	11.83	-8.07	0.02	0.22	8.07
36	J1147+4458	2016 May	176.902 222	44.981 712	12.97	-8.12	0.06	0.33	8.12
37	J1158+0531	2017 Feb	179.717 239	5.533 084	11.31	-8.0	-0.19	0.4	8.0
38	J1207+2244	2014 May	181.779 633	22.746 382	12.68	-8.57	-0.79	5.01	8.61
39	J1210+0023	2016 May	182.732 407	0.398 417	10.93	-7.98	-0.08	0.16	7.98
40	J1216-0244	2016 Apr	184.249 405	-2.73986	13.48	-7.92	-0.28	0.49	7.92
41	J1221+0907	2016 May	185.389 404	9.121 344	11.73	-7.92	-0.46	1.33	7.93
42	J1225-0452	2016 May	186.373 611	-4.870966	11.86	-7.44	-1.47	2.45	7.58
43	J1226+2323	2016 May	186.578 995	23.388 212	11.6	-8.2	-0.44	4.04	8.22
44	J1228+2519	2016 May	187.126 694	25.326 597	12.33	-8.03	-0.03	0.42	8.03
45	J1231+1232	2016 May	187.750 168	12.544 04	11.66	-7.97	-0.13	0.48	7.97
46	J1231+5243	2016 Nov	187.989 731	52.729 076	11.32	-8.12	0.15	0.4	8.12
47	J1234+4201	2016 May	188.587 86	42.032 703	12.2	-8.09	0.09	0.49	8.09
48	J1237+1922	2014 May	189.444 473	19.380 432	11.9	-7.9	-0.53	3.68	7.92
49	J1253+0753		193.442 032	7.8953	12.28	-7.87	-0.19	0.64	7.87
50	J1305+2815	2014 May	196.395 02	28.252 928	12.8	-7.97	0.04	0.79	7.97
51	J1313-0552		198.379 898	-5.87012	14.11	23.8	-34.18	70.73	41.65
52	J1345+0513	2016 May	206.460 266	5.218 417	11.45	-5.33	-1.19	6.15	5.46

**Table A1**  
(Continued)

No.	Name LAMOST	Obs.Date Y-m	R.A. (deg.)	Decl. (deg.)	G_Gaia (mag.)	x (kpc)	y (kpc)	z (kpc)	$R_{GC}$ (kpc)
53	J1350+0819	2016 May	207.564 835	8.321 019	11.75	-7.84	-0.05	0.39	7.84
54	J1352+2646	2014 May	208.003 876	26.778 688	12.5	-7.14	0.6	4.36	7.17
55	J1353+2021	2016 May	208.311 493	20.365 349	13.12	-7.85	0.03	0.53	7.85
56	J1359+2112	2016 May	209.888 535	21.216 253	12.74	-7.83	0.05	0.6	7.83
57	J1401+2659	2014 May	210.328 186	26.997 553	13.25	-7.8	0.15	0.91	7.8
58	J1404+3222	2016 May	211.127 502	32.378 613	11.97	-7.93	0.11	0.43	7.93
59	J1404+4111	2016 May	211.038 742	41.192 013	12.3	-7.97	0.17	0.46	7.97
60	J1410-0555	2014 May	212.511 81	-5.931057	12.35	-7.76	-0.11	0.34	7.76
61	J1414+1457	2016 May	213.634 415	14.963 419	10.75	-7.1	0.08	2.15	7.1
62	J1414+1721	2016 May	213.551 239	17.354 977	11.81	-7.55	0.08	1.17	7.55
63	J1423+0322	2016 May	215.859 329	3.378 907	11.92	-5.8	-0.4	3.53	5.81
64	J1424+3343	2016 May	216.124 832	33.718 842	12.46	-7.93	0.1	0.32	7.93
65	J1432+3755	2014 May	218.189 087	37.927 578	12.44	-6.74	2.86	7.06	7.32
66	J1434+3540	2016 May	218.682 159	35.672 359	11.82	-7.95	0.09	0.24	7.95
67	J1456+3122	2016 May	224.150 467	31.377 337	12.16	-7.03	1.12	2.84	7.12
68	J1459+0444	2016 May	224.957 291	4.737 969	12.08	-5.55	0.11	3.15	5.55
69	J1518+2544	2016 May	229.589 813	25.742 584	11.23	-7.32	0.55	1.37	7.34
70	J1523+0714	2016 May	230.911 789	7.248 231	11.69	-4.13	0.76	4.51	4.2
71	J1541+3009	2016 May	235.387 619	30.165 625	12.26	-7.84	0.18	0.31	7.84
72	J1548+2113	2017 Feb	237.247 849	21.224 567	10.41	-7.69	0.21	0.43	7.7
73	J1558+4149	2016 May	239.519 791	41.825 085	13.18	-7.81	0.44	0.56	7.82
74	J1629+1430	2014 May	247.258 27	14.514 119	12.35	-1.09	4.06	6.26	4.21
75	J1634+0206	2016 May	248.725 235	2.104 218	12.23	-6.0	0.64	1.26	6.04
76	J1657+3443	2014 May	254.381 317	34.724 27	11.82	-6.75	1.95	1.78	7.03
77	J1700+2159	2016 May	255.073 669	21.993 647	13.16	-5.04	2.7	2.68	5.72
78	J1718+5044	2016 May	259.700 562	50.739 422	12.1	-7.59	1.86	1.34	7.82
79	J1730+4143	2016 May	262.606 567	41.726 353	11.86	-7.12	2.07	1.42	7.42
80	J1731+2843	2016 May	262.939 758	28.721 027	11.97	-7.02	1.28	0.89	7.13
81	J1733+2633	2016 May	263.360 596	26.561 991	12.17	-7.0	1.2	0.83	7.1
82	J1757+2435	2016 May	269.463 348	24.596 937	11.48	-6.58	1.7	0.9	6.8
83	J1833+1309	2017 Aug	278.320 19	13.155 89	10.33	-7.82	0.17	0.04	7.82
84	J1954+5853	2017 Aug	298.683 807	58.898 689	11.08	-8.01	0.33	0.09	8.02
85	J1958+5533	2017 Aug	299.505 737	55.559 666	12.54	-7.99	0.54	0.13	8.01
86	J2109+1725	2017 Aug	317.491 73	17.428 883	10.47	-7.54	1.03	-0.42	7.61
87	J2216+0246	2015 Nov	334.149 841	2.771 391	12.45	-6.99	2.21	-2.2	7.33
88	J2216+2232	2015 Nov	334.163 757	22.547 327	12.02	-7.69	2.27	-1.21	8.02
89	J2217+2104	2015 Nov	334.460 785	21.076 998	13.02	-5.97	13.35	-7.52	14.62
90	J2221+0228	2015 Nov	335.453 461	2.479 126	12.48	-7.56	1.01	-1.04	7.63
91	J2242+2720	2015 Nov	340.689 606	27.340 151	12.8	-8.08	6.39	-3.31	10.31
92	J2347+2851	2017 Aug	356.998 26	28.858 528	10.87	-8.51	1.72	-1.12	8.68
93	J2350+0236	2017 Aug	357.744 995	2.604 288	12.1	-8.02	0.22	-0.34	8.02

## Appendix B

**Table B1**  
Stellar Parameters and Kinematic Parameters of our Sample

Name	$T_{\text{eff}}$ K	$\log g$ cgs	(Fe/H)	$\xi_{\text{mic}}$ ( $\text{km s}^{-1}$ )	Distance (kpc)	$U$ ( $\text{km s}^{-1}$ )	$V$ ( $\text{km s}^{-1}$ )	$W$ ( $\text{km s}^{-1}$ )	Group	Type
J0055+1857	5018	2.69	-2.31	1.48	0.803 859	-288	-195	-24	Halo	Turn-off
J0119+2425	6412	4.27	-2.56	1.64	0.274 582	78	-140	-37	Disk	Turn-off
J0131+4800	6141	4.03	-1.75	1.35	0.162 227	-170	-172	18	Halo	Turn-off
J0232+0545	6091	4.08	-2.16	1.11	0.928 764	-46	-202	77	Halo	Turn-off
J0244+0828	6472	4.39	-2.26	1.6	0.227 273	210	-157	-93	Halo	Turn-off
J0246+2643	6062	2.61	-2.5	3.7	1.537 988	112	-424	-378	Halo	Turn-off
J0326+0202	4827	1.92	-2.55	1.52	1.791 152	-118	-220	-20	Halo	Giant
J0352+0514	5909	4.22	-3.04	1.2	0.473 238	133	-150	-103	Halo	Turn-off
J0423+0538	6170	4.32	-1.96	1.31	0.286 747	-64	-131	-88	Disk	Turn-off
J0554+5235	5596	2.21	-1.95	2.3	3.475 843	-301	-505	-17	Halo	Turn-off
J0626+6032	5926	3.77	-2.18	1.3	1.179 663	-173	-226	160	Halo	Turn-off
J0637+4308	6366	4.11	-2.62	1.55	0.460 532	-98	-391	55	Halo	Turn-off
J0643+5111	5354	3.31	-2.39	1.23	1.199 328	-90	-400	-96	Halo	Turn-off
J0643+5934	4967	2.09	-2.46	1.71	1.494 322	-110	-114	7	Disk	Giant
J0828+0037	6104	3.48	-2.05	1.65	0.695 991	-190	-310	-57	Halo	Turn-off
J0832+2450	6161	3.92	-2.25	1.5	0.507 949	46	-266	74	Halo	Turn-off
J0834+2307	5361	3.39	-2.57	1.58	0.755 915	-42	-162	90	Halo	Turn-off
J0845+0150	6310	4.01	-2.22	1.8	0.704 473	87	-246	223	Halo	Turn-off
J0913+0726	6094	4.44	-1.94	1.34	0.356 697	81	-179	-55	Halo	Turn-off
J0924+2651	6201	3.98	-2.46	1.5	0.459 348	16	-80	-206	Halo	Turn-off
J0934-0108	5095	2.69	-2.4	1.49	1.260 24	-220	-7	-194	Halo	Turn-off
J0934-0259	6095	4.38	-1.79	1.3	0.333 957	-120	-170	-12	Halo	Turn-off
J0948+0000	6106	2.59	-2.47	3.1	2.127 66	92	-312	-129	Halo	Turn-off
J1014+0547	5851	3.95	-1.91	1.31	0.523 588	21	-358	-95	Halo	Turn-off
J1017+3755	5229	2.58	-2.91	1.85	2.4888	-165	-232	-66	Halo	Turn-off
J1044-0358	6319	4.02	-2.02	1.66	0.678 564	71	-199	-39	Halo	Turn-off
J1050+2135	6175	4.29	-2.24	1.27	0.239 716	-10	-93	71	Disk	Turn-off
J1101+2031	5241	2.87	-2.48	1.45	0.900 09	-91	-413	-64	Halo	Turn-off
J1109+0754	4502	1.19	-3.14	1.88	7.204 611	222	-181	-164	Halo	Giant
J1118-0650	4585	1.17	-3.32	2.14	4.926 108	-72	-95	68	Disk	Giant
J1123+0937	5959	4.45	-2.26	0.83	0.341 857	182	-280	73	Halo	Turn-off
J1123+3217	6275	4.45	-1.64	1.38	0.280 765	-123	-112	23	Disk	Turn-off
J1135+3100	6289	4.22	-2.68	1.61	0.427 972	17	-174	-48	Halo	Turn-off
J1137+4413	6241	4.07	-2.09	1.52	0.486 642	-17	-158	117	Halo	Turn-off
J1144+4032	5658	4.17	-2.47	0.79	0.231 508	2	-299	27	Halo	Turn-off
J1147+4458	5798	4.56	-2.42	0.56	0.351 853	-92	-418	-75	Halo	Turn-off
J1158+0531	5555	3.61	-2.31	1.39	0.442 556	226	-143	-19	Halo	Turn-off
J1207+2244	4743	1.8	-2.76	1.88	5.107 252	-36	-9	28	Disk	Giant
J1210+0023	5982	4.39	-2.09	1.01	0.177 955	149	-343	-86	Halo	Turn-off
J1216-0244	6104	4.4	-1.94	1.06	0.572 639	-128	-150	4	Halo	Turn-off
J1221+0907	5131	2.63	-2.27	1.4	1.409 642	304	-214	-9	Halo	Turn-off
J1225-0452	4872	1.9	-2.57	1.92	2.909 514	-91	-289	137	Halo	Giant
J1226+2323	4911	1.62	-2.35	1.94	4.070 004	3	-494	90	Halo	Giant
J1228+2519	6312	4.25	-1.77	1.27	0.418 953	277	-318	6	Halo	Turn-off
J1231+1232	6259	3.93	-2.32	0.85	0.495	38	-18	26	Disk	Turn-off
J1231+5243	5755	3.67	-1.98	1.38	0.442 419	-1	-50	-132	Disk	Turn-off
J1234+4201	6118	4.02	-1.98	1.34	0.504 388	53	-299	-129	Halo	Turn-off
J1237+1922	4908	1.81	-2.96	1.8	3.723 008	140	-140	-100	Halo	Giant
J1253+0753	5750	3.73	-3.96	1.2	0.682 967	172	-136	20	Halo	Turn-off
J1305+2815	6122	3.86	-2.74	1.52	0.788 519	-105	-116	46	Disk	Turn-off
J1313-0552	4643	2.16	-4.25	2.02	84.745 76	-1293	-1695	-84	Halo	Giant
J1345+0513	4614	1.17	-2.6	2.09	6.811 989	43	-296	-44	Halo	Giant
J1350+0819	6140	4.0	-2.32	1.7	0.420 84	22	-279	-74	Halo	Turn-off
J1352+2646	4730	1.73	-2.96	1.95	4.482 295	-156	-169	-67	Halo	Giant



**Table B1**  
(Continued)

Name	$T_{\text{eff}}$ K	$\log g$ cgs	(Fe/H)	$\xi_{\text{mic}}$ ( $\text{km s}^{-1}$ )	Distance (kpc)	$U$ ( $\text{km s}^{-1}$ )	$V$ ( $\text{km s}^{-1}$ )	$W$ ( $\text{km s}^{-1}$ )	Group	Type
J1353+2021	6009	4.25	-2.69	1.34	0.551 846	-61	-160	-233	Halo	Turn-off
J1359+2112	6364	3.83	-2.02	1.65	0.630 716	-144	-380	8	Halo	Turn-off
J1401+2659	6044	3.88	-2.82	1.5	0.945 18	-38	-183	-13	Halo	Turn-off
J1404+3222	6302	3.81	-1.86	1.54	0.447 908	-69	-77	-45	Disk	Turn-off
J1404+4111	6109	4.07	-1.89	1.35	0.493 925	58	-107	-97	Disk	Turn-off
J1410-0555	6205	4.73	-3.12	1.5	0.426 603	25	-189	49	Halo	Turn-off
J1414+1457	4787	1.69	-2.49	2.01	2.337 541	-61	-362	-103	Halo	Giant
J1414+1721	5176	2.64	-2.28	1.54	1.257 703	-206	-273	20	Halo	Turn-off
J1423+0322	4566	1.05	-2.68	1.96	4.180 602	-80	-247	-79	Halo	Giant
J1424+3343	6039	4.41	-1.85	1.25	0.347 645	91	-223	14	Halo	Turn-off
J1432+3755	4585	1.34	-3.12	2.08	7.722 008	-176	-301	170	Halo	Giant
J1434+3540	5876	4.37	-1.91	1.51	0.263 317	-54	-369	-55	Halo	Turn-off
J1456+3122	4827	1.86	-2.75	1.63	3.205 128	119	-199	-83	Halo	Giant
J1459+0444	4725	1.75	-2.59	1.82	3.998 401	-285	-101	-271	Halo	Giant
J1518+2544	5567	2.4	-1.95	2.16	1.626 281	53	-238	-7	Halo	Turn-off
J1523+0714	4715	1.25	-2.45	2.17	5.988 024	-450	-427	188	Halo	Giant
J1541+3009	6052	4.24	-1.81	1.21	0.392 603	253	-206	83	Halo	Turn-off
J1548+2113	5220	2.85	-1.84	1.46	0.570 386	88	-124	-45	Disk	Turn-off
J1558+4149	6396	4.11	-1.77	1.33	0.734 646	-106	-392	-64	Halo	Turn-off
J1629+1430	4669	1.07	-3.09	2.3	10.172 939	127	-254	-80	Halo	Giant
J1634+0206	5347	2.41	-2.0	1.87	2.450 38	118	-219	94	Halo	Turn-off
J1657+3443	4880	1.99	-2.65	2.27	2.917 153	-57	-254	91	Halo	Giant
J1700+2159	5657	2.33	-2.34	2.06	4.821 601	243	-269	-211	Halo	Turn-off
J1718+5044	5485	2.46	-2.41	2.16	2.329 373	-130	-199	-22	Halo	Turn-off
J1730+4143	4935	2.06	-2.38	1.75	2.656 042	-221	-96	6	Halo	Giant
J1731+2843	5117	2.45	-2.01	1.6	1.843 318	109	-250	-6	Halo	Turn-off
J1733+2633	5073	2.65	-3.04	1.6	1.768 034	27	11	36	Disk	Turn-off
J1757+2435	5803	2.31	-2.33	2.8	2.386 066	-133	-53	51	Disk	Turn-off
J1833+1309	5462	3.54	-2.39	1.15	0.248 701	282	-160	-86	Halo	Turn-off
J1954+5853	5992	3.52	-1.9	1.64	0.340 692	-114	-177	6	Halo	Turn-off
J1958+5533	6286	4.02	-2.2	1.73	0.554 847	57	-370	-11	Halo	Turn-off
J2109+1725	4957	2.13	-2.41	1.68	1.203 514	195	-384	-47	Halo	Giant
J2216+0246	4784	2.06	-2.45	1.9	3.274 394	-51	-220	-93	Halo	Giant
J2216+2232	4875	2.12	-2.64	1.86	2.595 38	18	-296	177	Halo	Giant
J2217+2104	4507	1.21	-3.64	2.4	15.455 951	-118	-243	-223	Halo	Giant
J2221+0228	5219	2.86	-2.95	1.55	1.511 259	27	-121	95	Disk	Turn-off
J2242+2720	4698	1.58	-3.59	2.11	7.199 424	97	-479	-70	Halo	Giant
J2347+2851	4881	1.79	-2.19	1.81	2.115 059	-13	-287	29	Halo	Giant
J2350+0236	6171	4.18	-2.92	1.6	0.403 063	19	-261	-194	Halo	Turn-off

## Appendix C

### Sodium Abundance of the Stars






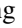

**Table C1**  
Sodium Abundances of our Sample

Name	A(5889) LTE	A(5895) LTE	(Na/Fe) LTE	err	A(5889) NLTE	A(5895) NLTE	(Na/Fe) NLTE	err
J0055+1857	4.03	4.11	0.21	0.06	3.53	3.56	-0.32	0.02
J0119+2425	3.31	3.33	-0.29	0.01	3.07	3.15	-0.5	0.06
J0131+4800	4.62	4.56	0.17	0.04	4.02	4.0	-0.41	0.01
J0232+0545	4.28	4.19	0.23	0.06	3.69	3.7	-0.32	0.01
J0244+0828	3.82	3.75	-0.13	0.05	3.43	3.47	-0.46	0.03
J0246+2643	3.55	3.47	-0.16	0.06	3.26	3.27	-0.41	0.01
J0326+0202	3.44	3.4	-0.2	0.03	2.93	2.97	-0.67	0.03
J0352+0514	2.84		-0.29		2.66		-0.47	
J0423+0538	4.49	4.51	0.29	0.01	3.88	3.98	-0.28	0.07
J0554+5235	5.1	4.84	0.75	0.18	4.32	4.21	0.05	0.08
J0626+6032	4.95	5.06	1.02	0.08	4.34	4.4	0.38	0.04
J0637+4308	3.45	3.37	-0.14	0.06	3.17	3.18	-0.38	0.01
J0643+5111	4.22	4.22	0.44	0.0	3.66	3.64	-0.13	0.01
J0643+5934	3.85	3.95	0.19	0.07	3.31	3.41	-0.35	0.07
J0828+0037	4.5	4.32	0.29	0.13	3.85	3.8	-0.3	0.04
J0832+2450	4.06	4.13	0.18	0.05	3.56	3.69	-0.3	0.09
J0834+2307	3.72	3.68	0.1	0.03	3.2	3.26	-0.37	0.04
J0845+0150	4.16	4.03	0.15	0.09	3.64	3.67	-0.3	0.02
J0913+0726	4.57	4.53	0.32	0.03	4.01	3.98	-0.24	0.02
J0924+2651	3.8	3.62	0.0	0.13	3.36	3.34	-0.36	0.01
J0934-0108	3.97	3.92	0.18	0.04	3.43	3.42	-0.35	0.01
J0934-0259	4.72	4.75	0.36	0.02	4.16	4.18	-0.21	0.01
J0948+0000	3.69	3.63	-0.04	0.04	3.35	3.4	-0.33	0.04
J1014+0547	4.71	4.8	0.5	0.06	4.14	4.2	-0.09	0.04
J1017+3755	4.02	4.0	0.75	0.01	3.44	3.51	0.22	0.05
J1044-0358	4.7	4.69	0.55	0.01	3.99	4.1	-0.11	0.08
J1050+2135	4.08	4.02	0.12	0.04	3.55	3.63	-0.34	0.06
J1101+2031	3.95	3.97	0.27	0.01	3.37	3.46	-0.28	0.06
J1109+0754	3.27	3.09	0.15	0.13	2.85	2.74	-0.24	0.08
J1118-0650	2.35	2.31	-0.52	0.03	2.14	2.16	-0.7	0.01
J1123+0937	4.55	4.56	0.65	0.01	4.05	4.04	0.14	0.01
J1123+3217	4.54	4.46	-0.03	0.06	3.95	3.97	-0.57	0.01
J1135+3100	3.81	3.68	0.26	0.09	3.42	3.42	-0.07	0.0
J1137+4413	4.31	4.22	0.19	0.06	3.75	3.76	-0.33	0.01
J1144+4032	3.77	3.77	0.07	0.0	3.37	3.4	-0.32	0.02
J1147+4458	3.88	3.9	0.14	0.01	3.44	3.51	-0.28	0.05
J1158+0531	4.09	4.21	0.29	0.08	3.53	3.67	-0.26	0.1
J1207+2244	3.53	3.46	0.09	0.05	3.01	3.03	-0.39	0.01
J1210+0023	4.24	4.21	0.15	0.02	3.71	3.72	-0.37	0.01
J1216-0244	4.45	4.47	0.23	0.01	3.92	3.95	-0.3	0.02
J1221+0907	4.26	4.27	0.37	0.01	3.67	3.67	-0.23	0.0
J1225-0452	3.75	3.83	0.19	0.06	3.23	3.3	-0.34	0.05
J1226+2323	4.25	4.28	0.45	0.02	3.63	3.68	-0.17	0.04
J1228+2519	4.75	4.82	0.39	0.05	4.11	4.2	-0.25	0.06
J1231+1232	3.93	3.93	0.08	0.0	3.4	3.52	-0.39	0.08
J1231+5243	4.74	4.87	0.62	0.09	4.18	4.23	0.02	0.04
J1234+4201	5.12	5.15	0.95	0.02	4.46	4.51	0.3	0.04
J1237+1922	3.51	3.36	0.23	0.11	3.02	3.02	-0.19	0.0
J1253+0753	2.04		-0.17		2.0		-0.21	
J1305+2815	3.25	3.17	-0.22	0.06	2.99	2.99	-0.44	0.0
J1313-0552	1.86		-0.06		1.83		-0.09	
J1345+0513	3.77	3.76	0.2	0.01	3.33	3.33	-0.24	0.0

**Table C1**  
(Continued)

Name	A(5889) LTE	A(5895) LTE	(Na/Fe) LTE	err	A(5889) NLTE	A(5895) NLTE	(Na/Fe) NLTE	err
J1350+0819	3.76	3.61	-0.17	0.11	3.33	3.31	-0.53	0.01
J1352+2646	3.37	3.23	0.09	0.1	2.9	2.88	-0.32	0.01
J1353+2021	3.29	3.29	-0.19	0.0	3.0	3.08	-0.44	0.06
J1359+2112	4.25	4.23	0.09	0.01	3.7	3.75	-0.43	0.04
J1401+2659	2.76	2.75	-0.6	0.01	2.59	2.61	-0.75	0.01
J1404+3222	5.21	5.18	0.89	0.02	4.43	4.38	0.1	0.04
J1404+4111	4.73	4.64	0.41	0.06	4.06	4.01	-0.25	0.04
J1410-0555	3.59	3.53	0.51	0.04	3.37	3.37	0.32	0.0
J1414+1457	4.22	4.13	0.5	0.06	3.63	3.54	-0.1	0.06
J1414+1721	4.22	4.15	0.3	0.05	3.59	3.56	-0.32	0.02
J1423+0322	3.64	3.55	0.11	0.06	3.25	3.14	-0.3	0.08
J1424+3343	4.56	4.53	0.23	0.02	3.99	4.01	-0.32	0.01
J1432+3755	3.16	3.07	0.07	0.06	2.76	2.76	-0.29	0.0
J1434+3540	4.61	4.65	0.37	0.03	4.1	4.11	-0.16	0.01
J1456+3122	3.49	3.37	0.01	0.08	3.01	2.95	-0.44	0.04
J1459+0444	3.66	3.65	0.08	0.01	3.17	3.18	-0.41	0.01
J1518+2544	4.88	4.75	0.6	0.09	4.16	4.08	-0.1	0.06
J1523+0714	3.76	3.6	-0.04	0.11	3.26	3.18	-0.5	0.06
J1541+3009	4.71	4.71	0.35	0.0	4.12	4.11	-0.25	0.01
J1548+2113	4.2	4.09	-0.19	0.08	3.61	3.51	-0.77	0.07
J1558+4149	4.53		0.13		3.9		-0.5	
J1629+1430	3.0	2.9	-0.13	0.07	2.68	2.65	-0.42	0.02
J1634+0206	4.61	4.54	0.41	0.05	3.94	3.84	-0.28	0.07
J1657+3443	3.45	3.49	-0.05	0.03	2.98	3.05	-0.51	0.05
J1700+2159	4.22	3.98	0.27	0.17	3.64	3.57	-0.23	0.05
J1718+5044	4.18	4.03	0.35	0.11	3.49	3.46	-0.29	0.02
J1730+4143	4.04	4.01	0.24	0.02	3.43	3.45	-0.35	0.01
J1731+2843	4.29	4.23	0.1	0.04	3.7	3.67	-0.48	0.02
J1733+2633	2.58	2.59	-0.55	0.01	2.34	2.41	-0.76	0.05
J1757+2435	4.32	3.98	0.31	0.24	3.76	3.66	-0.19	0.12
J1833+1309	4.03	4.11	0.29	0.06	3.5	3.6	-0.23	0.07
J1954+5853	4.62	4.59	0.34	0.02	3.93	3.97	-0.32	0.03
J1958+5533	3.84	3.72	-0.19	0.08	3.44	3.45	-0.53	0.01
J2109+1725	4.01	3.91	0.2	0.07	3.44	3.37	-0.36	0.05
J2216+0246	3.71	3.81	0.04	0.07	3.19	3.28	-0.49	0.06
J2216+2232	3.63		0.1		3.1		-0.43	
J2217+2104	3.19	3.17	0.65	0.01	2.8	2.9	0.32	0.07
J2221+0228	2.8	2.7	-0.47	0.07	2.52	2.53	-0.7	0.01
J2242+2720	2.12	2.22	-0.41	0.07	2.01	2.13	-0.51	0.08
J2347+2851	4.36	4.35	0.38	0.01	3.84	3.78	-0.17	0.04
J2350+0236	3.07	3.02	-0.2	0.04	2.89	2.9	-0.36	0.01

## ORCID iDs

S. A. Alexeeva  <https://orcid.org/0000-0002-8709-4665>  
 Gang Zhao  <https://orcid.org/0000-0002-8980-945X>  
 Shuai Liu  <https://orcid.org/0000-0001-5193-1727>  
 Hongliang Yan  <https://orcid.org/0000-0002-8609-3599>  
 Haining Li  <https://orcid.org/0000-0002-0389-9264>  
 Tianyi Chen  <https://orcid.org/0000-0002-6448-8995>  
 Huawei Zhang  <https://orcid.org/0000-0002-7727-1699>  
 Jianrong Shi  <https://orcid.org/0000-0002-0349-7839>

## References

- Alexeeva, S. A., Pakhomov, Y. V., & Mashonkina, L. I. 2014, *AstL*, **40**, 406  
 Andrievsky, S. M., Spite, M., Korotin, S. A., et al. 2007, *A&A*, **464**, 1081  
 Aoki, W., Li, H., Matsuno, T., et al. 2022, *ApJ*, **931**, 146  
 Baumüller, D., Butler, K., & Gehren, T. 1998, *A&A*, **338**, 637  
 Beers, T. C., & Christlieb, N. 2005, *ARA&A*, **43**, 531  
 Bensby, T., Feltzing, S., & Oey, M. S. 2014, *A&A*, **562**, A71  
 Butler, K., & Giddings, J. 1985, Newsletter on the Analysis of Astronomical Spectra, No. 9, University of London, arXiv:0805.0554  
 Cayrel, R., Depagne, E., Spite, M., et al. 2004, *A&A*, **416**, 1117  
 Cui, X.-Q., Zhao, Y.-H., Chu, Y.-Q., et al. 2012, *RAA*, **12**, 1197  
 Frebel, A., & Norris, J. E. 2015, *ARA&A*, **53**, 631  
 Gaia Collaboration, Prusti, T., de Bruijne, J. H. J., et al. 2016, *A&A*, **595**, A1  
 Gaia Collaboration, Vallenari, A., & Brown, A. G. A. 2022, arXiv:2208.00211  
 Gehren, T. 1979, *A&A*, **75**, 73  
 Gehren, T., Shi, J. R., Zhang, H. W., Zhao, G., & Korn, A. J. 2006, *A&A*, **451**, 1065  
 Griffith, E. J., Johnson, J. A., Weinberg, D. H., et al. 2023, *ApJ*, **944**, 47  
 Gustafsson, B., Edvardsson, B., Eriksson, K., et al. 2008, *A&A*, **486**, 951  
 Helmi, A. 2020, *ARA&A*, **58**, 205  
 Johnson, D. R. H., & Soderblom, D. R. 1987, *AJ*, **93**, 864  
 Kobayashi, C., Karakas, A. I., & Lugaro, M. 2020, *ApJ*, **900**, 179  
 Kobayashi, C., Umeda, H., Nomoto, K., Tominaga, N., & Ohkubo, T. 2006, *ApJ*, **653**, 1145  
 Kochukhov, O. 2018, BinMag: Widget for comparing stellar observed with theoretical spectra, Astrophysics Source Code Library, record, ascl:1805.015  
 Li, H., Aoki, W., Matsuno, T., et al. 2022, *ApJ*, **931**, 147  
 Li, H., Tan, K., & Zhao, G. 2018, *ApJS*, **238**, 16  
 Liu, X.-W., Zhao, G., & Hou, J.-L. 2015, *RAA*, **15**, 1089  
 Lombardo, L., Bonifacio, P., François, P., et al. 2022, *A&A*, **665**, A10  
 Mashonkina, L., Jablonka, P., Sitnova, T., Pakhomov, Y., & North, P. 2017, *A&A*, **608**, A89  
 McWilliam, A., Preston, G. W., Sneden, C., & Shtetman, S. 1995, *AJ*, **109**, 2736  
 Nissen, P. E., & Gustafsson, B. 2018, *A&Ar*, **26**, 6  
 Noguchi, K., Aoki, W., Kawanomoto, S., et al. 2002, *PASJ*, **54**, 855  
 Reggiani, H., Meléndez, J., Kobayashi, C., Karakas, A., & Placco, V. 2017, *A&A*, **608**, A46  
 Reggiani, H., Schlafman, K. C., Casey, A. R., & Ji, A. P. 2020, *AJ*, **160**, 173  
 Rybicki, G. B., & Hummer, D. G. 1991, *A&A*, **245**, 171  
 Sato, B., Kambe, E., Takeda, Y., Izumiura, H., & Ando, H. 2002, *PASJ*, **54**, 873  
 Spite, M., & Spite, F. 1978, *A&A*, **67**, 23  
 Tsybal, V., Ryabchikova, T., & Sitnova, T. 2019, in ASP Conf. Ser. 518, Physics of Magnetic Stars, ed. D. O. Kudryavtsev, I. I. Romanyuk, & I. A. Yakunin (San Francisco, CA: ASP), 247  
 Venn, K. A., Irwin, M., Shetrone, M. D., et al. 2004, *AJ*, **128**, 1177  
 Vincenzo, F., Thompson, T. A., Weinberg, D. H., et al. 2021, *MNRAS*, **508**, 3499  
 Yan, H., Li, H., Wang, S., et al. 2022, *The Innovation*, **3**, 100224  
 Zhao, G., Chen, Y.-Q., Shi, J.-R., et al. 2006, *ChJAA*, **6**, 265  
 Zhao, G., Mashonkina, L., Yan, H. L., et al. 2016, *ApJ*, **833**, 225  
 Zhao, G., Zhao, Y.-H., Chu, Y.-Q., Jing, Y.-P., & Deng, L.-C. 2012, *RAA*, **12**, 723